comptes rendus palevol

2022 • 21 • 9

The potential and limits of *Thin-Plate Spline* retrodeformation on asymmetrical objects: simulation of taphonomic deformations and application on a fossil sample of limb long bones

Romain PINTORE, Arnaud DELAPRÉ, Rémi LEFEBVRE, Léo BOTTON-DIVET, Alexandra HOUSSAYE & Raphaël CORNETTE

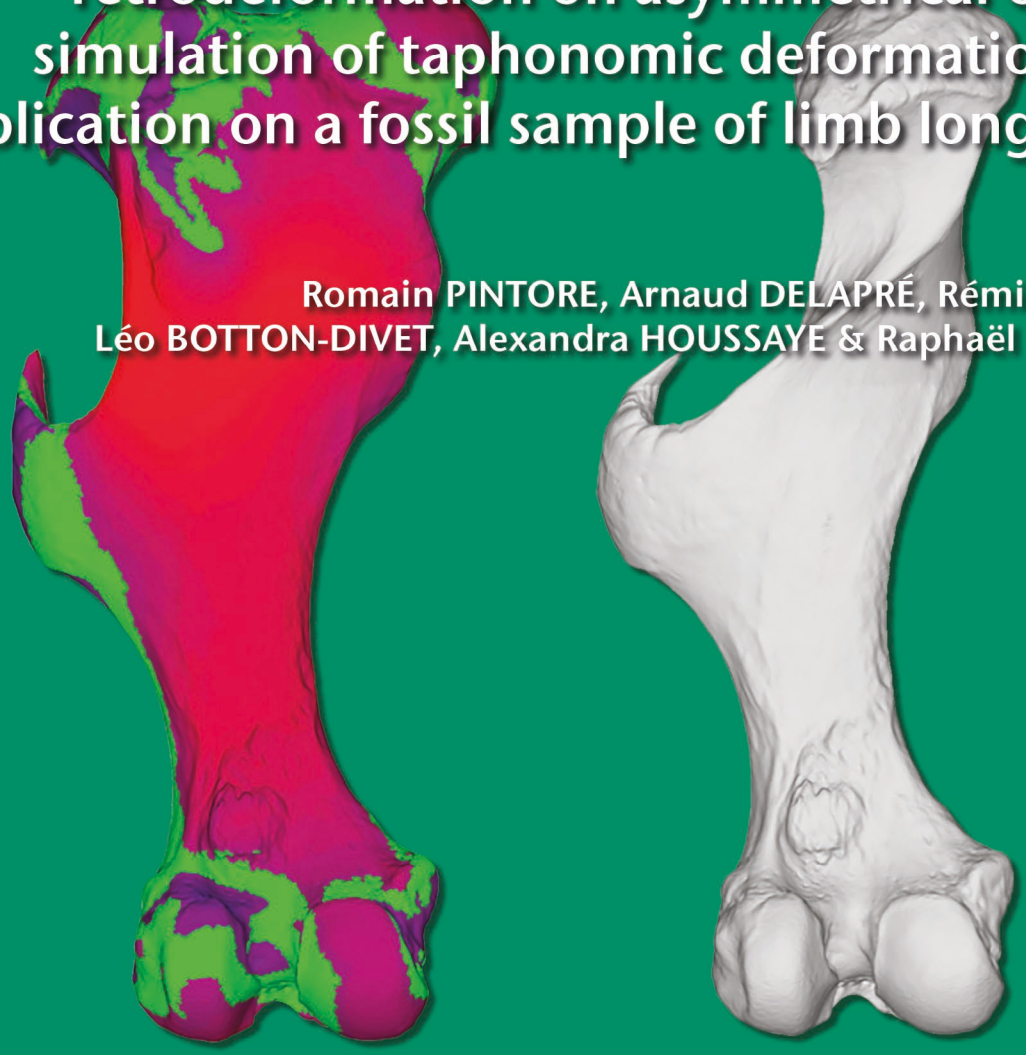

art. 21 (9) — Published on 8 March 2022
www.cr-palevol.fr

PUBLICATIONS SCIENTIFIQUES

Couverture / *Cover*:
Made from the Figures of the article.

Comptes Rendus Palevol est indexé dans / Comptes Rendus Palevol *is indexed by:*
– Cambridge Scientific Abstracts
– Current Contents® Physical
– Chemical, and Earth Sciences®
– ISI Alerting Services®
– Geoabstracts, Geobase, Georef, Inspec, Pascal
– Science Citation Index®, Science Citation Index Expanded®
– Scopus®.

Les articles ainsi que les nouveautés nomenclaturales publiés dans *Comptes Rendus Palevol* sont référencés par / *Articles and nomenclatural novelties published in* Comptes Rendus Palevol *are registered on:*
– ZooBank® (http://zoobank.org)

Comptes Rendus Palevol est une revue en flux continu publiée par les Publications scientifiques du Muséum, Paris et l'Académie des sciences, Paris
Comptes Rendus Palevol *is a fast track journal published by the Museum Science Press, Paris and the Académie des sciences, Paris*

Les Publications scientifiques du Muséum publient aussi / *The Museum Science Press also publish:*
Adansonia, ***Geodiversitas***, ***Zoosystema***, ***Anthropozoologica***, ***European Journal of Taxonomy***, ***Naturae***, ***Cryptogamie*** **sous-sections** ***Algologie***, ***Bryologie***, ***Mycologie***.

L'Académie des sciences publie aussi / *The Académie des sciences also publishes:*
Comptes Rendus Mathématique, ***Comptes Rendus Physique***, ***Comptes Rendus Mécanique***, ***Comptes Rendus Chimie***, ***Comptes Rendus Géoscience***, ***Comptes Rendus Biologies***.

Diffusion – Publications scientifiques Muséum national d'Histoire naturelle
CP 41 – 57 rue Cuvier F-75231 Paris cedex 05 (France)
Tél.: 33 (0)1 40 79 48 05 / Fax: 33 (0)1 40 79 38 40
diff.pub@mnhn.fr / https://sciencepress.mnhn.fr

Académie des sciences, Institut de France, 23 quai de Conti, 75006 Paris.

ISSN (imprimé / *print*): 1631-0683/ ISSN (électronique / *electronic*): 1777-571X

The potential and limits of *Thin-Plate Spline* retrodeformation on asymmetrical objects: simulation of taphonomic deformations and application on a fossil sample of limb long bones

Romain PINTORE
UMR 7179, Mécanismes adaptatifs et Évolution, Muséum national d'Histoire naturelle, Centre national de la Recherche scientifique, case postale 55, 57 rue Cuvier, F-75231 Paris cedex 05 (France)
romain.pintore@edu.mnhn.fr (corresponding author)

Arnaud DELAPRÉ
UMR 7205, Institut de Systématique, Évolution, Biodiversité (ISYEB), Muséum national d'Histoire naturelle, CNRS, Sorbonne Université, EPHE, Université des Antilles, CP 50, 57 rue Cuvier, 75005 Paris (France)
arnaud.delapre@mnhn.fr

Rémi LEFEBVRE
UMR 7179, Mécanismes adaptatifs et Évolution, Muséum national d'Histoire naturelle, Centre national de la Recherche scientifique, case postale 55, 57 rue Cuvier, F-75231 Paris cedex 05 (France)
remi.lefebvre@edu.mnhn.fr

Léo BOTTON-DIVET
AG Vergleichende Zoologie, Institut für Biologie, Humboldt Universität zu Berlin, Unter den Linden 6, 10099 Berlin (Germany)
leo.botton-divet@hu-berlin.de

Alexandra HOUSSAYE
UMR 7179, Mécanismes adaptatifs et Évolution, Muséum national d'Histoire naturelle, Centre national de la Recherche scientifique, case postale 55, 57 rue Cuvier, F-75231 Paris cedex 05 (France)
alexandra.houssaye@mnhn.fr

Raphaël CORNETTE
UMR 7205, Institut de Systématique, Évolution, Biodiversité (ISYEB), Muséum national d'Histoire naturelle, CNRS, Sorbonne Université, EPHE, Université des Antilles, CP 50, 57 rue Cuvier, 75005 Paris (France)
raphael.cornette@mnhn.fr

Submitted on 17 June 2020 | Accepted on 22 September 2020 | Published on 8 March 2022

urn:lsid:zoobank.org:pub:82922DEF-FAB7-4C04-ABE7-5EEFA156155C

Pintore R., Delapré A., Lefebvre R., Botton-Divet L., Houssaye A. & Cornette R. 2022. — The potential and limits of *Thin-Plate Spline* retrodeformation on asymmetrical objects: simulation of taphonomic deformations and application on a fossil sample of limb long bones. *Comptes Rendus Palevol* 21 (9): 191-205. https://doi.org/10.5852/cr-palevol2022v21a9

ABSTRACT
In this study, we suggest a method adapted to the retrodeformation of asymmetrical objects – such as limb bones – by quantitatively estimating the effectiveness of the *Thin-Plate Splines* (TPS) interpolation function as a retrodeformation tool. To do so, taphonomic deformations were first simulated on a single horse femur. The original bone was then used as a reference in order to drive the retrodeformation using anatomical landmarks. This approach, based on a single bone, enabled us to evaluate the performance of the retrodeformation procedure. Then, the same approach was performed on a sample of rhino femora but using a different specimen (from the same species) as the reference in order to account for morphological variation. We also added sliding semi-landmarks on anatomical curves. Finally, retrodeformation was applied on a sample of sauropodomorph dinosaur femora by building a mean shape based on several well-preserved fossil specimens. Results show that entirely flattened and stretched bones are more efficiently retrodeformed than bent and twisted bones. Introduction of morphological variation increased the efficiency of retrodeformation for bent and locally stretched bones. The application to the sample of fossils produced similar results but also highlighted the difficulty of retrodeforming bones with a combination of different deformations. TPS interpolation is an efficient tool of retrodeformation for asymmetrical objects, especially for bones with only one affine deformation such as flattening or stretching. Finding a threshold of landmark number to use for this process would be the next step because it would allow us to ensure the quality of retrodeformation while keeping available a reasonable number of landmarks in order to perform shape analysis on retrodeformed bones. Twisted and bent fossils are frequently discovered and we suggest that these kinds of deformations should be studied with caution, especially when combined with other types of taphonomic distortions.

KEY WORDS
Plateosauridae,
Rhinocerotoidae,
Equidae,
retrodeformation,
taphonomy,
3D geometric,
morphometrics,
limb bones.

RÉSUMÉ
Le potentiel et les limites de la rétrodéformation d'objets asymétriques par Thin-Plate Spline*: simulation de déformations taphonomiques et application sur un échantillon d'os longs fossiles.*
Dans cette étude, nous proposons une méthode de rétrodéformation adaptées aux objets asymétriques, comme les os des membres, en estimant l'efficacité de la fonction d'interpolation *Thin-Plate Splines* (TPS) comme outil de rétrodéformation. Des déformations taphonomiques sont simulées sur un seul et même fémur de cheval pour évaluer les performances de la procédure de rétrodéformation. L'os original est ensuite utilisé comme référence pour contrôler la rétrodéformation par l'intermédiaire de landmarks anatomiques. Cette approche basée sur un os unique permet d'évaluer les performances de la procédure de rétrodéformation. La même approche est ensuite appliquée sur deux fémurs de rhinocéros (de la même espèce) pour prendre en compte la variation morphologique. Des sliding semi-landmarks sur courbes anatomiques sont également utilisés. La rétrodéformation est finalement appliquée à un échantillon de fémurs de dinosaures sauropodomorphes en créant une forme moyenne basée sur différents spécimens fossiles en bon état de préservation. Les résultats démontrent que les os entièrement aplatis ou étirés sont plus efficacement rétrodéformés que les os courbés et tordus. L'introduction de variation morphologique a pour effet d'augmenter l'efficacité de la rétrodéformation pour les os courbés et avec un étirement localisé. L'application sur l'échantillon de fossiles donne des résultats similaires mais souligne également le fait que les combinaisons de différentes déformations sont moins efficacement rétrodéformées. L'interpolation par TPS est un outil de rétrodéformation efficace pour les objets asymétriques, tout particulièrement pour les os qui ne présentent qu'une seule déformation affine comme un écrasement ou un étirement. Il serait utile d'établir un nombre limite de landmarks pour assurer l'efficacité de la rétrodéformation tout en conservant une partie de l'échantillon de landmarks pour des études morphométriques sur les os rétrodéformés. Les fossiles sont souvent découverts courbés et tordus et nous suggérons que ces types de déformations soient plus profondément étudiés, surtout lorsqu'ils sont combinés avec d'autres types de déformations.

MOTS CLÉS
Plateosauridae,
Rhinocerotoidae,
Equidae,
rétrodéformation,
taphonomie,
géométrique 3D,
morphométrie,
os longs.

INTRODUCTION

Fossils generally undergo taphonomic processes before their discovery (Efremov 1940). Although these phenomena are informative regarding e.g. paleoecology, paleoenvironment, and geology (Brett & Baird 1986), the original biological information of the damaged fossil is altered (Webster & Hughes 1999; Hedrick & Dodson 2013; Hedrick *et al.* 2018). Of all these taphonomic degradations, plastic deformations – which refer to permanent and non-destructive degradations (Lee 1969; Lubarda & Lee 1981) – caused by geological phenomena are among the most frequently observed degradations. In this context, a wide variety of approaches aims to estimate the original shape of an altered fossil. Because the main goal is to apply the opposite taphonomic deformations on the deformed fossils, these approaches are termed "retrodeformation" processes.

Many retrodeformation methods consist of manually deforming a specimen in three dimensions (3D) by using a reference criterion. In fact, the popularization of 3D deformation techniques in multiple scientific areas (Sedeberg & Parry 1986; Zheng *et al.* 2017) can easily manipulate 3D models with the help of computers. However, manually deforming an object can induce a high degree of interpretation due to the high amount of uncertainty (Cunningham *et al.* 2014; Lautenschlager 2016). Using reference criteria, such as the bilateral symmetry of a skull, a conservative pattern along vertebrae or the known circular shape of an orbit (Arbour & Currie 2012; Cuff & Rayfield 2015; Vidal & Dìez Dìaz 2017; Cirilli *et al.* 2020; Dìez Dìaz *et al.* 2020), can however provide satisfying results. It is also possible to use a quantitative criterion in order to justify how to perform retrodeformation.

The first report of the quantification of tectonic deformations among rocks and fossils was published by Haughton in 1856. Harker published a similar study in 1885 to measure the effect of slaty cleavage on the deformation of fossils. Later, the first application of a quantified retrodeformation – inspired by the study of Harker (1885) – was published by Lake (1943) and relied on the manipulation of photographs. A rectangle was drawn around a picture of a distorted fossil. Then, light was projected through this picture according to an angle fitting the calculated amount of distortion. Finally, a new picture of the resulting projection was taken with a camera tilted at the opposite angle in order to remove any perspective effect. The operator knew that perspective effect was removed when the rectangle retrieved its original proportions. This approach allows us to both retrodeform an object using a quantified criterion (tectonic deformation) and to control the whole process with another criterion (proportions of the rectangle). Later, a wide variety of approaches reported how to study distorted fossils in two dimensions (2D) (Wellman 1962; Cooper 1990; Hughes & Jell 1992; Motani 1997) but the increasing use of 3D deformation techniques led researchers to investigate retrodeformation with a different scope.

3D deformation techniques allow us to perform an algorithmically driven retrodeformation on the whole geometry of an object. As in 2D, using anatomical criterion allows us to optimize the retrodeformation process. Such criteria – such as the shape of an object or the position of a structure of interest – allow us to ensure the quality of a retrodeformation process for a biological object. Forms of both extant and fossil organisms can be quantitatively studied using morphometric analyses. Because traditional morphometrics – i.e., linear distances, ratios and angles – can limit biological interpretations, because it does not capture the whole geometry of an object (Adams *et al.* 2013), geometric morphometrics (GM) was developed at the end of the 20th century. GM methods rely on the definition of landmark coordinates indicating the location of anatomical features.

Thus, landmarks can be used as anatomical criteria in order to justify the way retrodeformation is performed (Zollikofer 2002; Zollikofer *et al.* 2005; Lawing & Polly 2009; Molnar *et al.* 2012; Tschopp *et al.* 2013; Cunningham *et al.* 2014). Thin-Plate Spline (TPS) is an interpolation function widely used in computational graphics (Bookstein 1991). TPS (Bookstein 1991; Gunz *et al.* 2009; Mitteroecker & Gunz 2009) can be used to non-rigidly warp a target 3D landmark configuration or a 3D surface (Bookstein 1991; Gunz *et al.* 2009) according to a reference landmark configuration. Hence, TPS is used as a retrodeformation tool in order to restore the bilateral symmetry of palaeontological objects in different approaches which are: "Reflecting & Relabelling" (Angielczyk & Sheets 2007; Gunz *et al.* 2009) and "Non-Linear Symmetrisation", based respectively on bilateral landmarks (Ghosh *et al.* 2010; Tallman *et al.* 2014) or sliding semi-landmarks, which can be placed along curves and surfaces (Gunz & Mitteroecker 2013; Schlager *et al.* 2018). "Reflecting & Relabelling" is adapted for symmetrical objects that were deformed by a uniform shearing (Angielczyk & Sheets 2007; Gunz *et al.* 2009). "Non-Linear Symmetrisation" brings additional steps to the latter method in order to retrodeform symmetrical objects with bending (flexure) and compression (Ghosh *et al.* 2010; Tallman *et al.* 2014). These two methods rely on the use of anatomical landmarks only. However, anatomical landmarks can sometimes be difficult to locate on paleontological objects because of preservation issues. It was thus suggested to add sliding semi-landmarks (Schlager *et al.* 2018) in order to include in the retrodeformation procedure the distortion of asymmetry in anatomical regions lacking recognizable anatomical landmarks.

Nonetheless, these methods are only adapted to restore the bilateral symmetry of a 3D object (e.g. skulls, vertebrae) and are not currently optimized for asymmetrical objects (Hedrick *et al.* 2018). The solution usually suggested to restore the morphology of asymmetrical objects such as limb bones is to mirror the left or right element that is best preserved (Lautenschlager 2016). But, in many specimens, either the two sides are altered or one is missing. In such cases, and despite the need for estimating the original morphology of limb bones for functional analyses or museological purposes, no solution has been proposed to our knowledge.

Herein, we aim to estimate the potential and limits of the TPS function as a retrodeformation tool for asymmetrical objects using anatomical landmarks. The retrodeformation process consists of constraining a landmark configuration by a reference one. The surfaces located between anatomical landmarks are interpolated by following the landmark displacement. In order to do so, we applied different deformations on a single specimen to create a sample of limb bones with known deformations. We then performed TPS retrodeformation on this sample in order to estimate its efficiency for each type of deformation. This first part of the study sheds light on the power and limits of this method depending on the deformation type and intensity. The same method was then applied to a sample of different but morphologically close specimens in order to assess the effect of morphological variation on the TPS retrodeformation efficiency. Finally, an application was performed on a sample of fossilized prosauropod femora in order to test its reliability under real conditions.

TABLE 1. — List of the prosauropod femora used in this study. Left and right femora from SMNS 53537, SMNS 91296 (F10) and SMNS 91300 (F27) were most likely from the same individual respectively. *, specimens chosen for reference.

Taxon	Collection number	Side	Taphonomic deformations
Plateosaurus sp.	SMNS 91300 (F27)*	R	–
	SMNS13200a+e*	L	–
	SMNS 91297 (F14)*	L	–
	SMNS 91310 (F65)*	L	–
	GPITRE7288*	R	–
	SMNS 81914 (F8)	L	Medium twisting
	SMNS 91296 (F10)	L	High flattening on distal epiphysis
	SMNS 91300 (F27)	L	High flattening on proximal epiphysis
	SMNS 91310 (F65)	L	Stretching of diaphysis, medium twisting of distal epiphysis
	GPIT uncatalogued	L	Bending of proximal epiphysis
	SMNS6017	R	Bending of proximal epiphysis
	SMNS53537	L	Medium twisting, stretching of distal epiphysis
	SMNS 91296 (F10)	R	Global medium flattening
	SMNS 91306 (F48)	R	Medium twisting, flattening of distal epiphysis
	SMNS13200	R	Low twisting, stretching of distal epiphysis
	SMNS53537	R	Bending of distal diaphysis, stretching of distal epiphysis
	GPITRE7288	L	Low twisting
Plateosaurus gracilis	SMNS5715	L	Global high flattening, bending of distal epiphysis
Efraasia minor	SMNS12354c	L	Global high flattening
	SMNS57539	L	Global medium flattening, bending of diaphysis, low twisting of distal epiphysis
Plateosauridae indet.	SMNS12220	L	Global medium flattening, bending of distal epiphysis

MATERIAL

In the first part of this study, we used a left femur of the extant *Equus caballus* with no pathological deformation as a single reference for virtual simulations of taphonomic degradations. The unnumbered femur comes from the collections of the École Nationale Vétérinaire de Nantes (France). It was digitized in 3D using the Artec Eva surface scanner. The 3D reconstruction was performed using the Artec Studio Professional software (Artec 3D, v12.1.1.12).

In the second part of this study, we used two left femora of extant white rhinoceros with no pathological deformation. A left femur of *Ceratotherium simum* Burchell, 1817 (RMCA-RG35146) was used to perform virtual simulations of taphonomic deformations. A left femur of *Ceratotherium simum* (BICPC-NH.CON.37) was used as a reference to perform retrodeformations. For the scanning and 3D reconstruction, we followed the same protocol as for the horse femur.

In the third part of this study, the application to fossil bones, we used thirty-three femora of morphologically close basal sauropodomorph dinosaurs from the Triassic (Table 1; von Huene 1908; Moser 2003; Yates 2003; Lefebvre *et al.* 2020). All the bones were digitized using the same protocol mentioned above except left and right femora of specimen GPITRE7288, which were acquired by microtomography at the Institute for Geosciences of Tübingen, formerly known as Geologisch-Paläontologisches Institut Tübingen by H. Mallison (2010). Twelve femora were removed from the sample because they were affected by extreme types of deformation that were identified as the most problematic ones in the first part of our study. Five femora were identified as the best preserved ones because they are not affected by obvious taphonomic distortion. They were thus chosen as reference models for the retrodeformation step. The sixteen remaining femora were retained for applying retrodeformation (Table 1).

ABBREVIATIONS

Institutions

BCIPC	Powell Cotton Museum of Birchington-on-Sea, Birchington-on-Sea;
GPIT	Geologisch-Paläontologisches Institut Tübingen, Tübingen;
RMCA	Musée Royal de l'Afrique Centrale, Tervuren;
SMNS	Staatliches Museum für Naturkunde Stuttgart, Stuttgart.

Other abbreviations

GM	Geometric morphometrics;
TPS	Thin-Plate Spline.

METHODS

SIMULATION OF TAPHONOMIC DEGRADATIONS ON HORSE AND RHINO FEMORA

Choice of taphonomic deformation parameters

The first step in simulating taphonomic deformations on the two horse and rhino femora was to settle the taphonomic deformation's parameters. Frequently observed taphonomic deformations can be classified into types. We only considered unique deformations that do not result from a combination of different mechanical forces in order to limit the number of parameters. Data from the literature and the observation of fossil materials allowed us to define three main types of deformations: 1) flattening and stretching (Briggs & Williams 1981; Arbour & Currie 2012; Baert *et al.* 2014), 2) bending (Wahl 2009; Cuff & Rayfield 2015; Fanti *et al.* 2015) and 3) twisting (Colbert & Baird 1958; Nicholls & Russell 1985). Flattening and stretching are affine deformations that affect only distance parameters among bones, whereas bending and twisting also alter angles and are thus categorized as non-affine deformations (Zheng *et al.* 2017).

Flattening and stretching refer, respectively, to the contraction or the distension of the 3D surface along the antero-posterior,

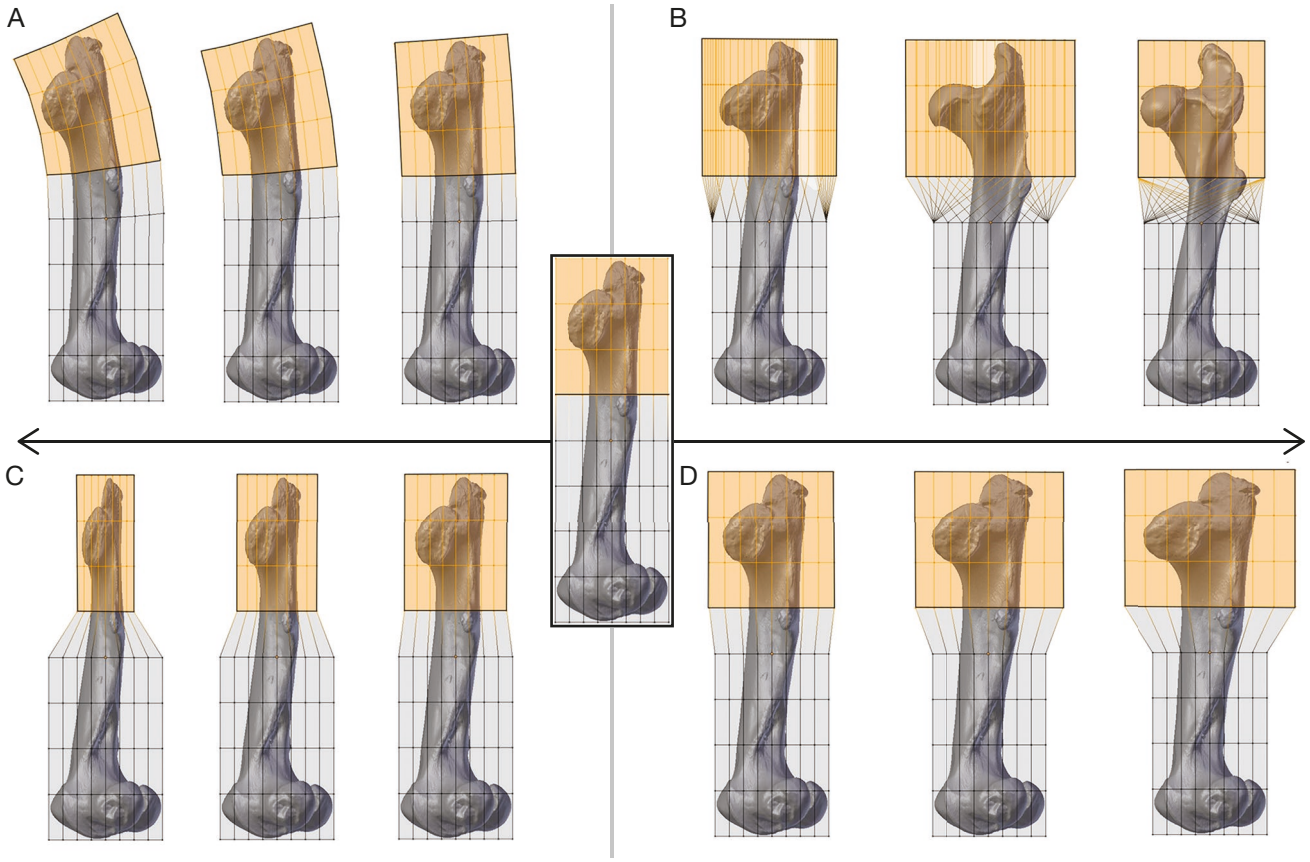

FIG. 1. — The different types of simulated deformations applied on the proximal epiphysis of the horse femur in lateral view. The bone at the centre is the original one. Arrows represent the increase of intensity of deformation from low, medium to high: **A**, bending; **B**, twisting; **C**, flattening; **D**, stretching.

the medio-lateral and the proximo-distal axis of the femur (Fig. 1C, D). This type of deformation is caused by the weight of sediment accumulation (Briggs & Williams 1981; Webster & Hughes 1999; Müller *et al.* 2018), tectonic processes (Hughes & Jell 1992) and trampling by other animals (Fanti *et al.* 2015). Bending refers to the folding of the surface along the antero-posterior or the medio-lateral axis of the femur (Fig. 1A). This type of deformation is caused by tectonic constraints that alter several layers of sediments during and/or after diagenesis (Wahl 2009; Fanti *et al.* 2015; Müller *et al.* 2018). Twisting refers to the rotation of the bone surface around its proximo-distal axis (Fig. 1B). This type of deformation is frequently observed but results from the occurrence of one of the deformations presented above on an object that already displays a natural twist. This suggests that post-mortem deformations such as compression can intensify the degree of this biological feature (Nicholls & Russell 1985). However, this type of deformation can also result from the combination of two forces applied in opposite directions (Thorson & Guthrie 1984).

We defined three different degrees of intensity for each type of deformation: low, medium and high (Fig. 1; Table 2). Intensities were defined based on the observation of fossil bones and on how much 3D meshes could be deformed without causing surface interpenetrations. These three degrees refer to the increasing effect of geological deformation on fossils. While the low intensity refers to fossils for which a retrodeformation step would not appear necessary, medium intensity indicates a visible effect of taphonomic processes. High intensity represents extreme situations where a retrodeformation step appears essential.

Then, different anatomical locations were defined in order to locally or globally apply each type of deformation. These locations were the proximal and distal epiphyses, the diaphysis, and the entirety of the bone. All of these deformations can be applied positively or negatively along each axis. Consequently, flattening and stretching are the same type of deformation applied in an opposite direction. Only medium and high intensities were applied to the epiphysis and the entirety of the two rhino femora. In total, one hundred and thirty-two 3D models were created based on the horse femur and fifty-two models were created for the two rhino femora (Table 2).

Application of the deformations

We applied deformations to the original 3D object using the Blender software (The Blender Foundation, v. 2.79) in order to simulate taphonomy. The 3D femur – from horse and rhino – was placed within a deformation grid (Joshi *et al.* 2007) to ensure the repeatability of the anatomical selection for each simulation. Boundaries between both epiphyses and the diaphysis were defined according to the most distal point of the third trochanter and the most proximal point of the condylar

Table 2. — The different parameters of deformation. Axis: **X**, medio-lateral, **Y**, antero-posterior; **Z**, proximo-distal.

Types	Bending	Twisting	Stretching	Flattening
Intensity	5 ; 15 ; 25°	10 ; 45 ; 90°	10 ; 30 ; 50%	
Localisations	Epiphysis and diaphysis		Epiphysis, diaphysis and entirety	
Axis	X ; Y	Z	X ; Y ; Z	
Directions	+ / -		+	-
Number (horse)	36	24	36	36
Number (rhinos)	8	8	18	18

crests. Thus, all parameters for all types of deformations were applied to a same anatomical location using the deformation grid (Fig. 1). Thirty-eight anatomical landmarks were defined and located on the horse femur following Hanot *et al.* (2017) using the Landmark software (Wiley *et al.* 2005, v. 3.0.0.6). 27 anatomical landmarks and 612 sliding semi-landmarks on curves (70 curves) were located on rhino femora following Mallet *et al.* (2019). The retrodeformation step was then performed through a TPS deformation using the function "tps3d" of the package Morpho (Schlager 2017) in R (R Core Team, v. 3.4.3). During this process, the deformed specimen's conformation was warped onto a reference conformation – the original horse femur and a rhino femur from the same species – using anatomical landmarks as fixed points. The displacement of anatomical landmarks drove the interpolation of the bone surfaces located between these landmarks. This surface interpolation was the morphological estimation used as retrodeformation. The deformation between the deformed femur and the reference was optimized in order to minimize the "bending energy" (Bookstein 1991; Mitteroecker & Gunz 2009).

Comparisons between retrodeformed and original bones

Consistencies and dissimilarities between undeformed and retrodeformed femora were quantified using the "meshDist" function of the package Morpho (Schlager 2017). This function measures the distances between each closest vertex of two different meshes. Then, the interval between the first and the third quartiles of these measures were selected as one representative measurement for each retrodeformed femur. Finally, results were graphically displayed using a combination of boxplots and density graphs with the types of deformation along the abscissa and their corresponding measurements along the ordinate using the package ggplot2 (Wickham 2009). The smaller the distance, the more efficient the retrodeformation is deemed to be.

Then, differences between interpolated surfaces of undeformed and retrodeformed femora – the original horse femur and another rhino femur from the same species – were graphically represented with heatmaps using the "meshDist" function (Schlager 2017). A threshold was defined in order to clearly delimit a difference between consistent and inconsistent surfaces. This threshold was defined using the smallest interval measured, which is 1.95 mm for the horse femur and 3 mm for rhino femora. Measures inferior to this value were referenced as neutral. When measures are superior to this threshold, the 3D surface is either in expansion or in compaction relative to the original bone. Although results for the horse femur provided information about the retrodeformation efficiency itself, results for the rhino femora added information about the effect of intraspecific morphological variation on the retrodeformation.

Application to a fossil sample

Because the sample was composed of left and right femora, all left femora were mirrored with Blender (The Blender Foundation, v. 2.79) using "mirror" and "flip directions" functions. 20 landmarks were defined and located with the Landmark software (Wiley *et al.* 2005, v. 3.0.0.6). Contrarily to previous cases, no reference was available for the retrodeformation step. Therefore, the five best preserved femora were selected in order to serve as a reference. A mean shape of these five femora was computed with a Generalized Procrustes Analysis (Rohlf & Slice 1990) using the functions "procSym" and its value "mshape" from the package Morpho (Schlager 2017). A few landmarks were missing on eight femora because of taphonomic destructions: SMNS 81914 (F8); SMNS 91297 (F14); SMNS 91300 (F27); Left SMNS 91310 (F65); SMNS 5715; SMNS 12354c; SMNS 6017; Right SMNS 53537. These missing landmark coordinates were interpolated with those of the reference shape by using TPS with the function "fixLMtps" of the package Morpho (Schlager 2017). Finally, the retrodeformation step was performed similarly as above by interpolating the shape of the 16 femora of the sample with the reference configuration, as in the third step of the "Target Deformation Protocol" by Cirilli *et al.* (2020). Heatmaps were not used for this chapter because deformed specimens were not created based on the same original one like it was the case for horse and rhino bones. The function "rotmesh.onto" of the package Morpho (Schlager 2017) was used to perform a Procrustes fit between the original bone and the retrodeformed one. Then, the function "deformGrid3d" of the package Morpho (Schlager 2017) was used to show the retrodeformation effectiveness by visualizing differences between the original and the retrodeformed bones.

RESULTS

Simulation of taphonomic degradations on horse femora

The smallest distance measured between undeformed and retrodeformed femur is 0.54 mm (0.1% of maximal height) whereas the greatest is 5.67 mm (1.2% of maximal height) (Fig. 2). Distances are lower for stretched, flattened and bent bones than for twisted ones (Fig. 2). Ranges (difference between minimum and maximum distances within each deformation type) are lower for stretched, flattened and bent bones than for twisted bones (Fig. 2). This means that measures of distances are more spread for twisted bones than for the other categories. The range increases from stretched to flattened to bent bones (Fig. 2). The median is centred for stretched, flattened and bent bones but is offset from the third

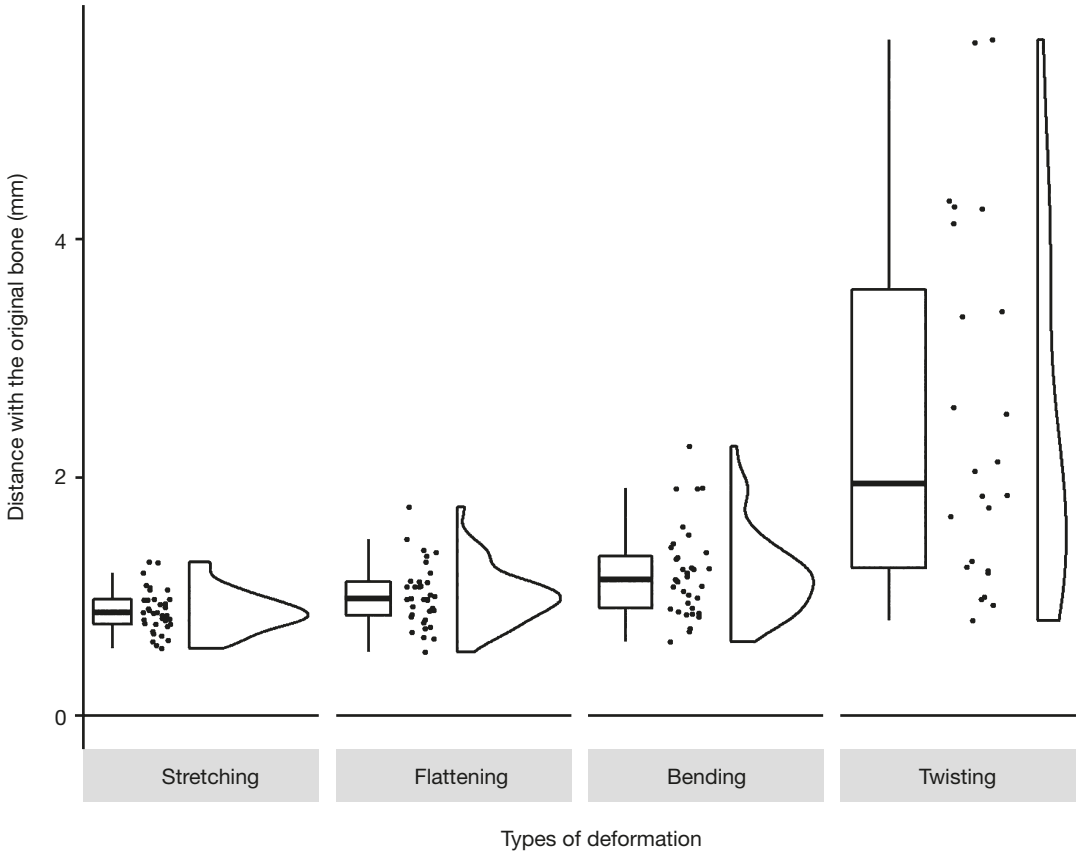

FIG. 2. — Measured distances for retrodeformed horse femora. The distances between the surfaces of the undeformed femur and the retrodeformed femora (ordinate) were sorted by types of deformations (abscissa). Dots represent each measurement and their variation along the abscissa was randomized for visibility. Boxplot and density curves allow us to visualize the distribution within each type of deformation.

quartile for twisted bones (Fig. 2). This means that there are more numerous high distances measured for twisted bones than for the other categories. The curve of density shows that most of the distances measured between undeformed and retrodeformed femora are concentrated below the median within each category of deformations, especially for stretched, flattened and bent bones (Fig. 2). It also shows that distances higher than the median are more spread than the lower distances (Fig. 2). This is also the case for twisted bones but at a higher scale (Fig. 2). This means that low distances are similar, which is not the case for high distances.

Based on these results, it is possible to rank these different types of deformation from the most to the least efficient retrodeformations: 1) stretching; 2) flattening; 3) bending; and 4) twisting.

Distances vary mostly in accordance with both intensities and deformation types (Appendix 1). In fact, the best retrodeformed bones within each category are from low intensities. Distances for medium intensities are higher than those of low intensities except for flattened and stretched bones where they are comparable. Highest distances are always observed for high intensities.

Least efficient retrodeformations for each type of deformation are selected according to previous results in order to produce heatmaps (Fig. 3). No recurring inconsistencies of surfaces were identified on retrodeformed flattened and stretched horse femora. However, retrodeformations of bent and twisted bones have morphological differences from the original bone that seem to be related to the original deformations.

The least efficient retrodeformation of bent bone shows that the highest distances are localized toward the proximal epiphysis (Fig. 3A). Compaction and expansion are observed symmetrically on both medial and lateral sides of the folding angle, causing a shift of the proximal part of the diaphysis. The least efficient retrodeformation for twisted bone shows a full flattening of the diaphysis (Fig. 3B).

Simulation of taphonomic degradations on rhino femora

The smallest distance measured for rhino femora is 6.39 mm (1.2% of maximal height) whereas the greatest is 9.77 mm (2% of maximal height) (Fig. 3). The distances measured for stretched, flattened and bent bones are lower than for twisted bones (Fig. 4). The range (difference between minimum and maximum distances within each deformation type) is lower for stretched, flattened and bent bones than for twisted bones (Fig. 4). The range increases from bent to stretched to flattened bones (Fig. 4), indicating that measures of distances are more

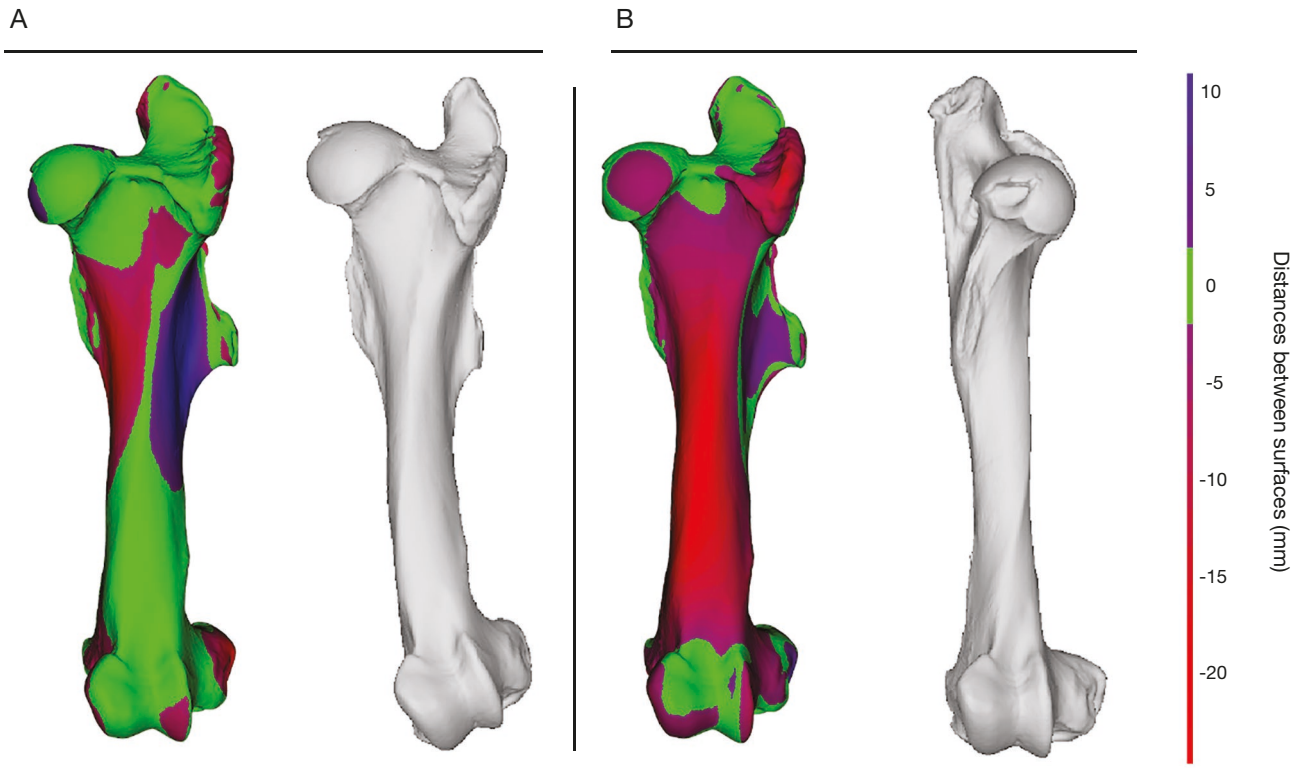

Fig. 3. — Heatmaps of highest distances measured for horse retrodeformed femora from (**A**) bending and (**B**) twisting. The distances between the surfaces of the undeformed and a retrodeformed femora were shown directly onto the surface of the original as heatmaps. Bones with the simulated taphonomic deformations were represented in **grey**.

spread for twisted bones than for the other categories. The median is closer to the third quartile than to the first quartile for bent, stretched and twisted bones (Fig. 4). This is the opposite case for flattened bones. This suggests that there are more high distances measured for flattened bones than for the other categories. The curve of density shows that most of the distances measured between original and retrodeformed bones within each category of deformations are concentrated around the median for stretched bones, higher than the median for flattened and bent bones, and lower than the median for twisted bones (Fig. 4). This shows that high distances are more similar for flattened and stretched bones than for twisted bones and that distances for stretched bones have a normal distribution.

Although bent bones have the lowest range, the curve of density shows that most of the distances measured in this category are still higher than those for stretched and flattened bones. Therefore, it is possible to rank the different types of deformations from the most to the least efficient retrodeformations: 1) stretching; 2) flattening; 3) bending and (4) twisting.

Least efficient retrodeformations for each type of deformation are selected according to previous results in order to produce heatmaps (Fig. 5). No recurring inconsistencies were identified on bent, flattened and stretched rhino femora. However, twisted bones display a flattening along the full extent of the diaphysis (Fig. 5).

Results show that the efficiency of TPS retrodeformation depends on the type of taphonomic deformation that altered the bone. Stretched and flattened bones are more likely to lead to a more efficient retrodeformation than bent and especially twisted bones. This is also the case when the retrodeformation is applied using two morphologically different bones from the same species. This shows that intraspecific morphological variation does not affect the efficiency of retrodeformation and its dependency to deformation types. However, distances measured across all types of deformations are globally higher for rhinos than horses. This means that using a different specimen as a reference – which is ultimately the aim of the TPS retrodeformation – introduces more uncertainties in the process of estimating the original morphology of a bone, which is always the case for fossil bones. The combination of anatomical landmarks and sliding semi-landmarks offers a better covering of the overall biological shape of an object (Botton-Divet *et al.* 2015; Goswami *et al.* 2019). This means that less interpolation will be computed between the deformed bone and the reference. Results show that retrodeformation effectiveness remains consistent between the two iterations as the retrodeformation between different closely related specimens – rhino femora – still produces the same trend of results than with the original specimen as a reference – the horse femur.

Application to a fossil sample of prosauropods

Bones affected by twisting, which was identified as the worst managed deformation in the first part, were retrodeformed for left SMNS 91296 (F10), SMNS 13200, SMNS 91306 (F48), left GPIT_RE 7288 and SMNS 81914 (F8). As a result, a slight flattening of the diaphysis is observable on SMNS 81914 (F8),

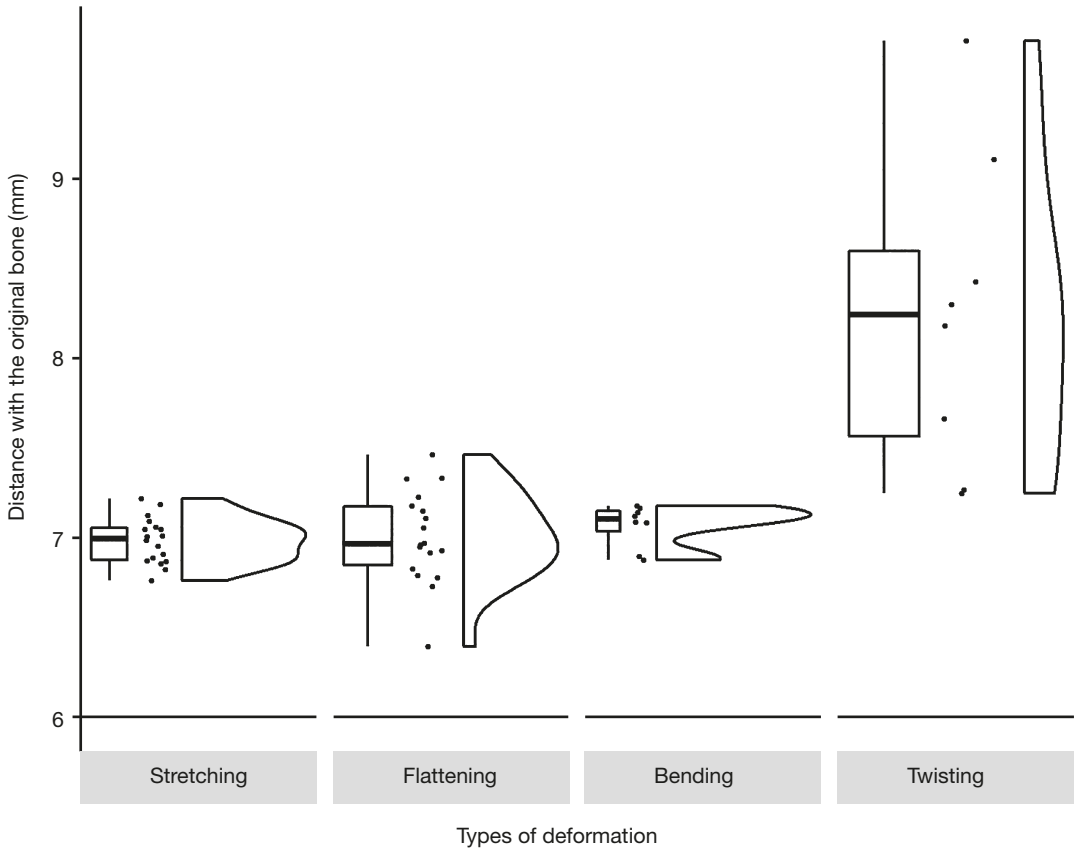

Fig. 4. — Measured distances for retrodeformed rhino bones. The distances between the surfaces of the undeformed femur and the retrodeformed ones using a different undeformed femur (ordinate) were sorted by types of deformations (abscissa). Dots represent each measurement and their variation along the abscissa was randomized for visibility. Boxplot and density plot allow us to visualize the distribution within each type of deformation.

left SMNS 91296 (F10) and left GPIT_RE7288 (Fig. 6). Bent bones were also retrodeformed for right SMNS 53537 and GPITN uncatalogued. However, SMNS 6017, SMNS5715, left SMNS57539 and SMNS 12220 seem problematic regarding this deformation (Fig. 6). Entirely flattened bones were retrodeformed for right SMNS 91296 (F10) and SMNS 5715 but were more problematic for SMNS 57539, SMNS12220 and SMNS12354c. Partially flattened bones were also retrodeformed for left SMNS 91300 (F27), F48 and left and right SMNS 91296 (F10) (Fig. 6). Stretched bones were also retrodeformed for right SMNS 91310 (F65), SMNS 53537 and SMNS 13200 (Fig. 6). Every deformed bone shows a noticeable difference after the retrodeformation process except for SMNS 5715, SMNS 57539 and SMNS 12220, whereas SMNS 12354c shows a greater retrodeformation than the others (Fig. 6).

DISCUSSION

Retrodeformation effectiveness depends on deformation types

Retrodeformations of horse femora were more efficient for flattened, stretched and bent bones than for twisted ones (Fig. 2). Bent bones were less efficiently retrodeformed in the study of horse femora. In fact, twisting and bending are localized on a particular area of the bone and cannot be applied globally like flattening and stretching. Moreover, retrodeformations of flattened and stretched bones were best managed when these deformations were applied to the entire bone rather than to localized areas (Fig. 7). These elements suggest that the more homogeneous – or affine – the deformation is, the more efficient the retrodeformation is deemed to be. The same results were observed with the study of rhino femora except for globally stretched bones, which were not better managed than locally stretched ones.

Retrodeformations of twisted and bent bones always triggered recurring inconsistencies between the original and retrodeformed bones (Fig. 4), which was not the case for flattened and stretched bones. These recurring inconsistencies are linked to the deformation parameters. In the case of twisted bones, the more important the twisting angle is on the deformed bone, the more flattened the shaft is on the retrodeformed bone. In the case of bent bones, the orientation of the bending angle affected the localisation of compactions and expansions of surfaces on the lateral or medial sides on the retrodeformed bone. Because of these recurring patterns of inconsistencies, these observations allow us to specify the limitations of surface interpolation in the case of these two types of taphonomic deformations. Moreover, these surface inconsistencies are located on areas that bear the

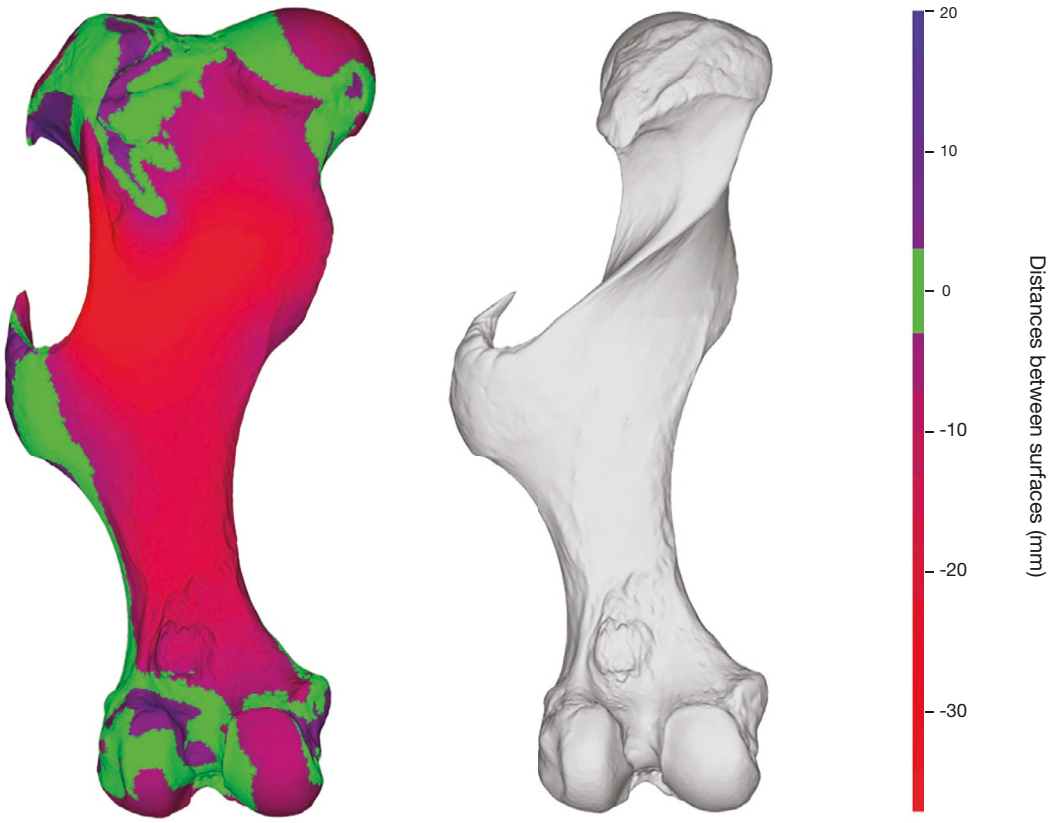

Fig. 5. — Heatmap of highest distances measured for rhino retrodeformed bones (twisting). The distances between the surfaces of the undeformed femur and the retrodeformed one using a different undeformed femur were shown directly on the surface of the original as heatmaps. Bone with the simulated taphonomic deformations are represented in **grey**.

fewest landmarks. This observation shows that surfaces with only a few landmarks were more interpolated than surfaces with more. The same results were observed on twisted rhino femora but not on bent ones.

The effect of morphological variation on retrodeformation efficiency

The fact that the same results were observed using a different femur from the same species as a reference shows that the retrodeformation is still operational when introducing intraspecific morphological variation. This similarity suggests that the morphological diversity in the sample of sauropodomorph femora would not negatively affect the retrodeformation efficiency. Furthermore, differences between results of horse and rhino femora are subtle: lowest distances measured are 0.1% and 1.2% of the maximal height of horse and rhino respectively. Despite being low, these differences also tell us about the effect of intraspecific morphological variation on the retrodeformation efficiency. Two main differences were observed between the results. Bent rhino femora did not produce recurring inconsistencies and globally stretched rhino femora were not more efficiently retrodeformed than locally stretched ones. This can be explained by the fact that intraspecific variability increases the morphological diversity and reduces the importance of taphonomic deformations in the measurements. Thus, the introduction of morphological diversity would lower the effect of taphonomic deformations on the retrodeformation efficiency, especially those caused by bending and localized stretching, as shown by results on rhino femora (Fig. 3). This aspect is of interest regarding the potential application of this methodology to a fossil sample, because it suggests that retrodeformation will be more efficient because there will always be morphological diversity in a real sample. However, it is sometimes not possible to select a reference bone from the same species as the deformed one. In that case, it remains important to select a reference that is morphologically as close as possible.

Application to a fossil sample

Stretched bones were retrodeformed consistently with observations from horse and rhino femora. No global stretching deformation was identified in this sample. Consistent with previous results, twisted bones were retrodeformed but with the appearance of a slight flattening of the diaphysis. These two types of deformation were retrodeformed with the same efficiency as in the study of horse and rhino femora.

Retrodeformation seems not efficient for SMNS 5715, SMNS 57539 and SMNS 12220 (Fig. 6A). Deformations identified on these bones were a combination of local bending and medium or high global flattening. These three bones are the only ones that bear this specific combination of deformations. This suggests that this specific combination leads to a non-efficient retrodeformation and that it should be studied with caution.

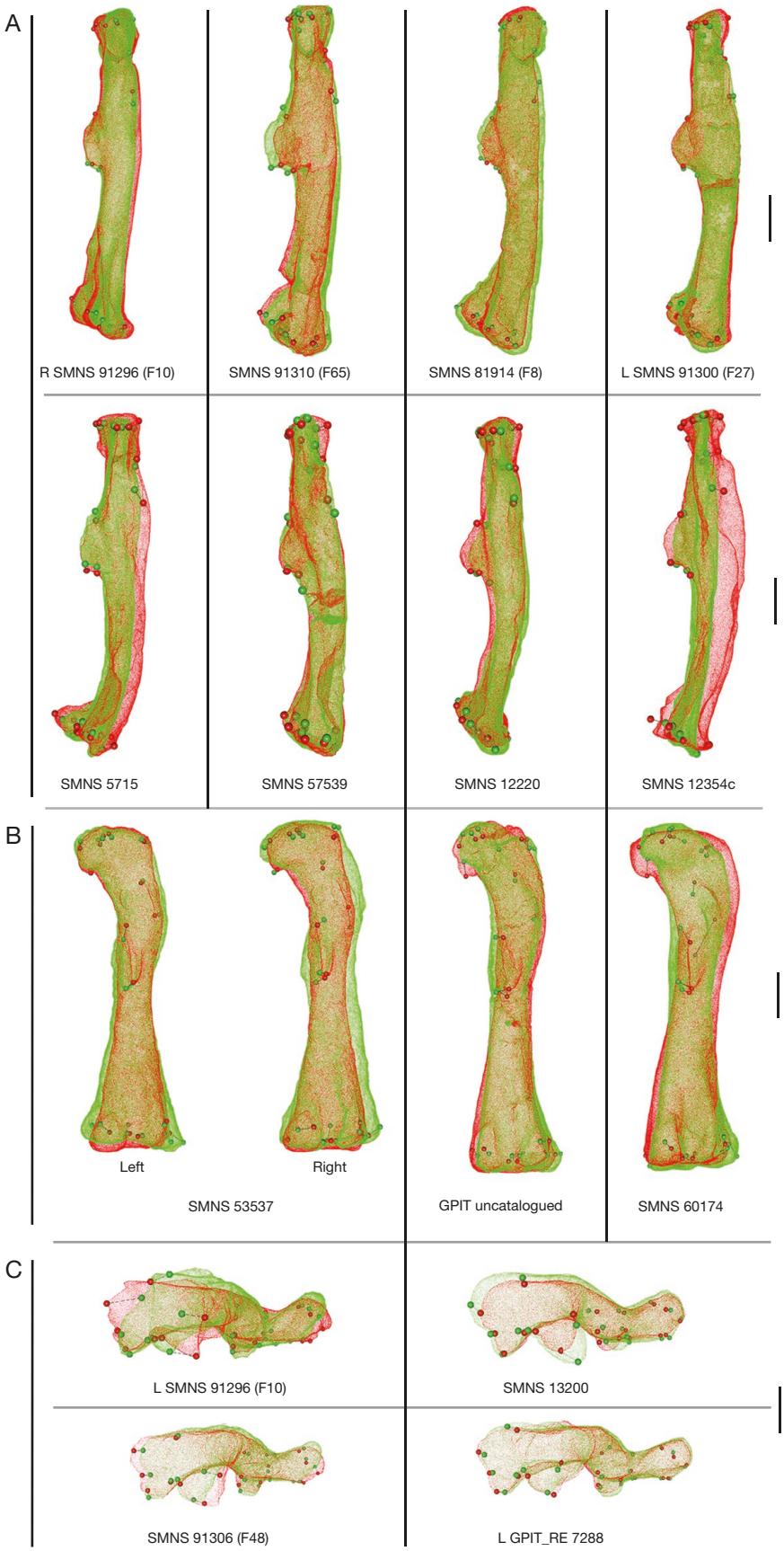

FIG. 6. — Retrodeformations of prosauropod femora in: **A**, lateral view; **B**, posterior view; **C**, 3D distal view. Original bones are shown in green whereas retrodeformed ones are in red. Landmarks of each bone are indicated with the same colours.

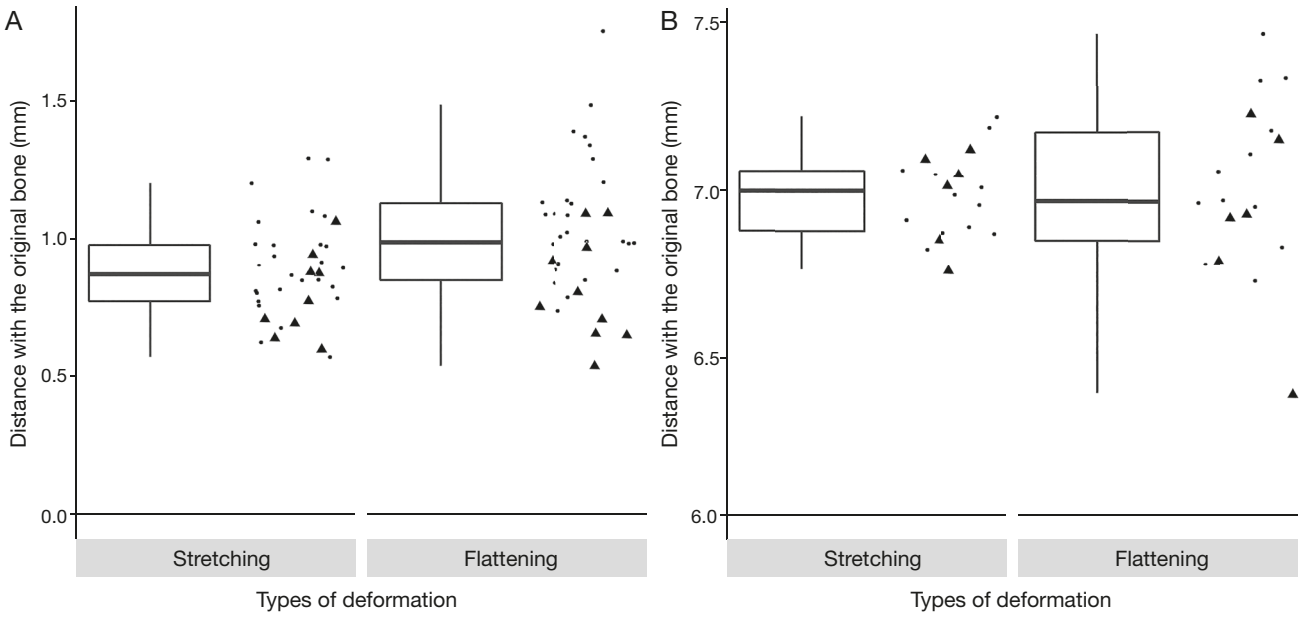

FIG. 7. — Measurements for stretched and flattened bones for (**A**) horse and (**B**) rhino femora. Dots represent each distance measurement for bones with global (**circles**) and local (**triangles**) deformations.

Because no combination of deformations was studied on horse and rhino femora, it is safer to warn about the efficiency of TPS retrodeformation in regard to combination of deformations in general.

Retrodeformation of SMNS12354c revealed a morphology that seems highly stretched compared to other bones (Fig. 6.A). This bone was diagnosed with a globally high flattening. Studies of horse and rhino femora showed that high intensity deformations were the least efficiently retrodeformed for each type of deformation. Thus, results are consistent even though this bone is the only one with an exaggerated retrodeformation. This phenomenon could be explained by the fact that the number of landmarks is lower than for horse and rhino femora. This could also result from a locally high taphonomic degradation on an area with a landmark that drove the interpolation with an intensity higher than required.

Left and right femora of SMNS53537 bear different taphonomic deformations even though they come from the same individual (Fig. 6; Table 1). This is probably because these bones were positioned differently when they underwent taphonomic deformation under the same geological constraint (Müller *et al.* 2018). The two retrodeformed bones of SMNS53537 show an overall resemblance that was not obvious before the retrodeformation was performed (Fig. 6B). This shows that the retrodeformation allowed us to remove the taphonomic component to highlight the biological information at the intra-individual level.

CONCLUSION

This study shows the capacity of estimating the original morphology of an asymmetrical object by the use of *Thin-Plate spline* deformation. Using a single bone deformed iteratively, we highlighted that flattening and stretching were efficiently retrodeformed with this approach, especially when they extended along the whole bone, leading to affine deformations. This is a promising result because these deformations are frequently observed among fossils. However, twisting of medium and high intensity as well as bending are complex taphonomic deformations that could be difficult to retrodeform. We recommend not to apply this type of retrodeformation to highly – or even moderately – twisted specimens. Results also showed that retrodeformation efficiency remained consistent between each iteration after introducing morphological variation and sliding semi-landmarks on curves. These different approaches widen the scope of application of retrodeformation by TPS to different cases. Specifying these aspects by defining a threshold of landmark density would also allow us to define a sub-sample of landmarks dedicated to retrodeformation and another one to perform geometric morphometric analysis.

Acknowledgements
We thank A. Profico (University of York, United Kingdom) and two anonymous reviewers and the associate editor, Lorenzo Rook for their helpful contribution to this study. We also thank all the curators of the visited institutions for granting access to the studied specimens: M. Comte, A. Borvon (École Nationale Vétérinaire de Nantes, France), R. Schoch (Staatliches Museum für Naturkunde of Stuttgart, Germany), I. Werneburg and J. Hinz (Geologisch-Paläontologisches Institut Tübingen, Germany), E. Gilissen (Royal Museum for Central Africa of Tervuren, Belgium), C. West, R. Jennings and M. Cobb (Powell Cotton Museum of Birchington-on-Sea, United-Kingdom). We thank H. Mallison (Palaeo3D) for providing 3D models

of prosauropod femora from the Geologisch-Paläontologisches Institut Tübingen. We also thank R. Allain, G. Billet, C. Mallet, C. Etienne, J. Bardin, (Muséum national d'Histoire naturelle, France) and P. Hanot (The Max Planck Institute for the Science of Human History, Germany) for constructive discussions and advice on data interpretation.

Funding

This work was funded by the European Research Council and is part of the GRAVIBONE project (ERC-2016-STG-715300). The funders had no role in study design, data collection and analysis, decision to publish, or preparation of the manuscript.

Grant disclosure

The following grant information was disclosed by the authors: This work was funded by the European Research Council and is part of the GRAVIBONE project (ERC-2016-STG-715300).

REFERENCES

ADAMS D. C., ROHLF F. J. & SLICE D. E. 2013. — A field comes of age: geometrics morphometrics in the 21st century. *Histrix, the Italian journal of Mammalogy* 24 (1): 7-14. https://doi.org/10.4404/hystrix-24.1-6283

ANGIELCZYK K. D. & SHEETS H. D. 2007. — Investigation of simulated tectonic deformation in fossils using geometric morphometrics. *Paleobiology* 33 (1): 125-148. https://doi.org/10.1666/06007.1

ARBOUR V. M. & CURRIE P. J. 2012. — Analyzing taphonomic deformation of Ankylosaurus skull using retrodeformation and finite element analysis. *PLoS ONE* 7: e39323. https://doi.org/10.1371/journal.pone.0039323

ARTEC 3D. 2018. — Artec Studio Professional. Santa Clara: Artec 3D. Available at https://www.artec3d.com/.

BAERT M., BURNS M. E. & CURRIE P. J. 2014. — Quantitative diagenetic analyses of Edmontosaurus regalis (Dinosauria: Hadrosauridae) postcranial elements from the Danek bonebed, upper cretaceous Horseshoe Canyon Formation, Edmonton, Alberta, Canada: implications for allometric studies of fossils organisms. *Canadian Journal of Earth Sciences* 51: 1007-1016. https://doi.org/10.1139/cjes-2014-0060

BLENDER 1995. — The Blender Foundation. Version 2.79.

BOOKSTEIN F. L. 1991. — *Morphometric tools for landmark data: geometry and biology*. Cambridge University Press, Cambridge, 456 p.

BOTTON-DIVET L., HOUSSAYE A., HERREL A., FABRE A.-C. & CORNETTE R. 2015. — Tools for quantitative form description; an evaluation of different software packages for semi-landmark analysis. *Peer J* 3: e1417. https://doi.org/10.7717/peerj.1417

BRETT C. E. & BAIRD G. C. — 1986. Comparative taphonomy: A key to paleoenvironmental interpretation based on fossil preservation. *PALAIOS* 1: 207-227.

BRIGGS D. E. G. & WILLIAMS S. H. 1981. — The restoration of flattened fossils. *Lethaia* 14: 157-164. https://doi.org/10.1111/j.1502-3931.1981.tb01918.x

CIRILLI O., MELCHIONNA M., SERIO C., BERNOR R. L., BUKHSIANIDZE M., LORDKIPANIDZE D., ROOK L., PROFICO A. & RAIA P. 2020. — Target Deformation of the *Equus stenonis* Holotype skull: A Virtual Reconstruction. *Frontiers in Earth Science* 8: 247. https://doi.org/10.3389/feart.2020.00247

COLBERT E. H. & BAIRD D. 1958. — Coelurosaur bone casts from the Connecticut Valley Triassic. *American Museum Novitates* 1901: 1-11. http://hdl.handle.net/2246/2486

COOPER R. A. 1990. — Interpretation of tectonically deformed fossils. *New Zealand Journal of Geology and Geophysics* 33 (2): 321-332. https://doi.org/10.1080/00288306.1990.10425690

CUFF A. R. & RAYFIELD E. J. 2015. — Retrodeformation and muscular reconstruction of ornithomimosaurian dinosaur crania. *Peer J* 3: e1093. https://doi.org/10.7717/peerj.1093

CUNNINGHAM J. A., RAHMAN I. A., LAUTENSCHLAGER S., RAYFIELD E. J. & DONOGHUE P. C. J. 2014. — A virtual world of paleontology. *Trend in Ecology and Evolution* 29 (6): 347-357. https://doi.org/10.1016/j.tree.2014.04.004

DÌEZ DÌAZ V., DEMUTH O. E., SCHWARZ D. & MALLISON H. 2020. — The Tail of the Late Jurassic Sauropod *Giraffatitan brancai*: Digital Reconstruction of Its Epaxial and Hypaxial Musculature, and Implications for Tail Biomechanics. *Frontiers in Earth Science* 8: 160. https://doi.org/10.3389/feart.2020.00160

EFREMOV J. A. 1940. — Taphonomy: New branch of paleontology. *Pan-American Geologist* 75: 81-93. http://serc.carleton.edu/resources/19358.html

FANTI F., CURRIE P. J. & BURNS M. E. 2015. — Taphonomy, age, and paleoecological implication of a new Pachyrhinosaurus (Dinosauria: Ceratopsidae) bonebed from the upper cretaceous (Campanian) Wapiti formation of Alberta, Canada. *Canadian Journal of Earth Sciences* 52: 250-260. https://doi.org/10.1139/cjes-2014-0197

GHOSH D., AMENTA N. & KAZHDAN M. 2010. Closed-form blending of local symmetries. *Eurographics Symposium on Geometry Processing* 29 (5): 1681-1688. https://doi.org/10.1111/j.1467-8659.2010.01777.x

GOSWAMI A., WATANABE A., FELICE R. N., BARDUA C., FABRE A. C. & POLLY P. D. 2019. — High-Density Morphometric Analysis of Shape and Integration: The Good, the Bad, and the Not-Really-a-Problem. *Integrative and Comparative Biology* 59 (3): 669-683. https://doi.org/10.1093/icb/icz120

GUNZ P., MITTEROECKER P., NEUBAUER S., WEBER G. W. & BOOKSTEIN F. L. 2009. — Principles for the virtual reconstruction of hominin crania. *Journal of Human Evolution* 57 (1): 48-62. https://doi.org/10.1016/j.jhevol.2009.04.004

GUNZ P. & MITTEROECKER P. 2013. — Semilandmarks: a method for quantifying curves and surfaces. *Histrix the Italian Journal of Mammalogy* 24 (1): 103-109. https://doi.org/10.4404/hystrix-24.1-6292

HANOT P., GUINTARD C., LEPETZ S. & CORNETTE R. 2017. — Identifying domestic horses, donkeys and hybrids from archaeological deposits: A 3D morphological investigation on skeletons. *Journal of Archaeological Science* 78: 88-98. https://doi.org/10.1016/j.jas.2016.12.002

HARKER A. 1885. — The cause of lsaty cleavage: Compression v. Shearing. *Geological Magazine* 2 (1): 15-17. https://doi.org/10.1017/S0016756800188223

HAUGHTON S. 1856. — On slaty cleavage and distorsion of fossils. *Philosophical Magazine* 12: 409-421. https://doi.org/10.1080/14786445608642208

HEDRICK B. P. & DODSON P. 2013. — Lujiatun Psittacosaurids: Understanding individual and taphonomic variation using 3D geometric morphometrics. *PLoS ONE* 8: e69265. https://doi.org/10.1371/journal.pone.0069265

HEDRICK B. P., SCHACHNER E. R., RIVERA G., DODSON P. & PIERCE S. E. 2018. — The effect of skeletal asymmetry on interpreting biologic variation and taphonomy in the fossil record. *Paleobiology* 45 (1): 154-166. https://doi.org/10.1017/pab.2018.42

HUGHES N. C. & JELL P. A. 1992. — A statistical/computer-graphic technique for assessing variation in tectonically deformed fossils and its application to Cambrian trilobites from Kashmir. *Lethaia* 25 (3): 317-330. https://doi.org/10.1111/j.1502-3931.1992.tb01401.x

HUENE F. VON. 1908. — Die Dinosaurier der europäischen Triasformation, mit Berücksichtigung der ausser–europäischen Vorkomnisse. *Geologie und Paläontologie Abhandlungen* 6: 345-419.

Joshi P., Meyer M., DeRose T., Green B. & Sanocki T. 2007. — Harmonic coordinates for character articulation. *ACM Transactions on Graphics* 26 (3): 1-9. https://doi.org/10.1145/1275808.1276466
Lake P. 1943. — Restoration of the original form of distorted specimens. *Geological magazine* 80 (4): 139-147. https://doi.org/10.1017/S0016756800076317
Lautenschlager S. 2016. — Reconstructing the past: methods and techniques for the digital restoration of fossils. *Royal Society of Open Sciences* 3 (10): 160342. https://doi.org/10.1098/rsos.160342
Lawing A. M. & Polly P. D. 2009. — Geometric morphometrics: recent applications to the study of evolution and development. *Journal of Zoology* 280 (1): 1-7. https://doi.org/10.1111/j.1469-7998.2009.00620.x
Lee E. H. 1969. — Elastic-plastic deformation at finite strains. *Journal of Applied Mechanics* 36 (1): 1-6. https://doi.org/10.1115/1.3564580
Lefebvre R., Allain R., Houssaye A. & Cornette R. 2020. — Disentangling biological variability and taphonomy: shape analysis of the limb long bones of the sauropodomorph dinosaur *Plateosaurus*. *PeerJ* 8: e9359. https://doi.org/10.7717/peerj.9359
Lubarda V. A. & Lee E. H. 1981. — A correct definition of elastic and plastic deformation and its computational significance. *Journal of Applied Mechanics* 48 (1): 35-40. https://doi.org/10.1115/1.3157589
Mallet C., Cornette R., Billet G. & Houssaye A. 2019. — Interspecific variation in the limb long bones among modern rhinoceroses – extent and drivers. *PeerJ* 7: e7647. https://doi.org/10.7717/peerj.7647
Mallison H. 2010. — The Digital *Plateosaurus I: Body Mass, Mass Distribution and Posture Assessed Using CAD and CAE on a Digitally Mounted Complete Skeleton. Palaeontologica Electronica* 13: 1-26.
Mitteroecker P. & Gunz P. 2009. — Advances in Geometric Morphometrics. *Evolutionary Biology* 36: 235-247. https://doi.org/10.1007/s11692-009-9055-x
Molnar J., Pierce S. E. & Hutchinson J. R. 2012. — Idealized landmark-based geometric reconstructions of poorly preserved fossil material: A case study of an early tetrapod vertebra. *Palaeontologica Electronica* 15: 1-18. https://doi.org/10.26879/274
Motani R. 1997. — New technique for retrodeforming tectonically deformed fossils, with an example for ichtyosaurian specimens. *Lethaia* 30 (3): 221-228. https://doi.org/10.1111/j.1502-3931.1997.tb00464.x
Moser M. 2003. — Plateosaurus engelhardti Meyer, 1837 (Dinosauria: Sauropodomorpha) from the Feuerletten (Middle Keuper; Upper Triassic) of Bavaria. 2003. *Zitteliana* Vol. B. 24: 1-188. https://doi.org/10.5282/ubm/epub.12711
Müller R. T., Garcia M. S., Da-Rosa Á. A. S. & Dias-da-Silva S. 2018. — Under pressure: Effect of sedimentary compression on the iliac morphology of early sauropodomorphs. *Journal of South American Earth Sciences* 88: 345-351. https://doi.org/10.1016/j.jsames.2018.09.005
Nicholls E. L. & Russell A. P. 1985. — Structure and function of the pectoral gridle and forelimb of Struthiomimus altus (Theropoda: Ornithomimidae). *Palaeontology* 28 (4): 643-677.
R Core Team. 2014. — R: a language and environment for statistical computing. Version 3.4.3. Vienna: R Foundation for Statistical Computing.
Rohlf F. J. & Slice D. 1990. — Extensions of the Procrustes method for the optimal superimposition of landmarks. *Systematic Biology* 39 (1): 40-59. https://doi.org/10.2307/2992207
Schlager S. 2017. — Statistical shape and deformation analysis. In Morpho and Rvcg–Shape Analysis, *in* Zheng G., Li S. & Szekely G. (eds), R: R-packages for geometric morphometrics, shape analysis and surface manipulations. *Academic Press*: 217-56.
Schlager S., Profico A., Di Vincenzo F. & Manzi G. 2018. — Retrodeformation of fossil specimens based on 3D bilateral semi-landmarks: Implementation in the R package "Morpho". *PLoS ONE* 13: e0194073. https://doi.org/10.1371/journal.pone.0194073
Sederberg T. W. & Parry S. R. 1986. — Free-form deformation of solid Geometric Models. *Proceedings of the 13th annual conference on Computer graphics and interactive techniques (SIGGRAPH '86)* 20 (4): 151-160. https://doi.org/10.1145/15922.15903
Tallman M., Amenta N., Delson E., Frost S. R., Ghosh D., Klukkert Z. S., Morrow A. & Sawyer G. J. 2014. — Evaluation of a new method of fossil retrodeformation by algorithmic symmetrization: Crania of Papionins (Primates, Cercopithecidae) as a test case. *PLoS ONE* 9: e100833. https://doi.org/10.1371/journal.pone.0100833
Thorson R. M. & Guthrie R. D. 1984. — River ice as a taphonomic agent: An alternative hypothesis for bone "artifacts". *Quaternary Research* 22 (2): 172-188. https://doi.org/10.1016/0033-5894(84)90038-3
Tschopp E., Russo J. & Dzemski G. 2013. — Retrodeformation as a test for the validity of phylogenetic characters: an example from diplodocid sauropod vertebrae. *Palaeontologia Electronica* 16: 1-23. https://doi.org/10.26879/312
Vidal D. & Díez Díaz V. 2017. — Reconstructing hypothetical sauropod tails by means of 3D digitization: *Lirainosaurus astibiae* as case of study. *Journal of Iberian Geology* 43: 293-305. https://doi.org/10.1007/s41513-017-0022-6
Wahl W. R. 2009. — Taphonomy of a nose drive: Bone and tooth displacement and mineral accretion in an Ichtyosaur skull. *Paludicola* 7: 107-116.
Webster M. & Hughes N. C. 1999. — Compaction-related deformation in Cambrian Olenelloid trilobites and its implications for fossil morphometry. *Journal of Paleontology* 73 (2): 355-371. https://doi.org/10.1017/S0022336000027827
Wellman H. W. 1962. — Graphical method for analysing fossil distorsion caused by tectonic deformation. *Geological Magazine* 99 (4): 348-352. https://doi.org/10.1017/S0016756800058453
Wickham H. 2009. — Ggplot2: create elegant data visualisations using the grammar of graphics. R package version 2.2.1.
Wiley D. F., Amenta N., Alcantara D. A., Ghosh D., Kil, Y. J., Delson E, Harcourt-Smith W., Rohlf F. J., St. John K. & Hamann B. 2005. — Evolutionary morphing. *Proceedings of IEEE Visualization:* 431-438.
Yates D. 2003. — The species taxonomy of the sauropodomorph dinosaurs from the Löwenstein (Norian, Late Triassic) formation of Germany. *Palaeontology* 46 (2): 317-337. https://doi.org/10.1111/j.0031-0239.2003.00301.x
Zheng G., Li S. & Székely G. 2017. — *Statistical Shape and Deformation Analysis: Methods, Implementation and Applications*. Academic Press, London, 488 p.
Zollikofer C. P. E. 2002. — A computational approach to Paleoanthropology. *Evolutionary Anthropology* 11 (S1): 64-67. https://doi.org/10.1002/evan.10059
Zollikofer C. P. E., Ponce de Leon M. S., Lieberman D. E., Guy F., David P., Likius A., Mackaye H. T., Vignaud P. & Brunet M. 2005. — Virtual cranial reconstruction of Sahelanthropus tchadensis. *Nature* 434: 755-759. https://doi.org/10.1038/nature03397

Submitted on 17 June 2020;
accepted on 22 September 2020;
published on 8 March 2022.

APPENDIX

APPENDIX 1. — Distances between the horse original bone and every retrodeformed one. All retrodeformed bones are plotted in abscissa with their associated distances with the original (inter-quartile distance) in ordinate. Types of deformation are represented by the **coloured geometrical shapes**. Intensities of deformations are figured by **rectangles** increasingly filled along abscissa.